Microcracking Resistance of 3D Printed Fibre Composites at Cryogenic Temperatures

Feng Huang [a], Wenkai Chang [a], Mohammad S Islam [a], Jiawei Wang [a], Bingnong Jiang [a], Zhibin Tan [b], Chun H. Wang [a*]

[a]

[a] School of Mechanical and Manufacturing Engineering, University of New South Wales, Sydney, NSW 2052, Australia

[b] Fordyno, Sydney, NSW 2065, Australia

[*] Corresponding author E-mail address: chun.h.wang@unsw.edu.au

Abstract

Thermoplastic composites present considerable promise for the 3D printing of cryogenic fuel storage tanks, offering enhanced recyclability and repairability compared to thermoset composites. However, a significant knowledge gap remains regarding their ability to withstand cryogenic environments without suffering ply cracking. This study investigates the microcracking behaviour of continuous carbon fibre reinforced thermoplastic (CFRTP) composites fabricated through extrusion-based 3D printing. The experimental results reveal that CFRTP composites printed at room temperature exhibit a remarkable ability to withstand an applied strain of 0.60% without ply cracking at liquid nitrogen temperature. This performance surpasses that of conventional carbon fibre reinforced epoxy composites, which typically experience ply cracking even with any applied strain. Some of microcracks were traced back manufacturing defects. The defects were found to be fused by a post-heat treatment at 180℃ for 60 min. Unexpectedly, however, the treatment reduced the ply-cracking strain to 0.40% at the liquid nitrogen temperature. Computational micromechanical modelling revealed that this unexpected decline in ply-cracking resistance resulted from the increased thermal residual stresses induced by the heat treatment. The findings of this study suggest that 3D-printed thermoplastic composites exhibit robust resistance to microcracking at cryogenic temperatures, making them a promising solution in the quest for sustainable lightweight cryogenic fuel storage solutions.

Keywords

Three-Dimensional Printing; Carbon Fibre Reinforced Polymer Composite; Cryogenic Application; Ply Cracking

1. Introduction

Lightweight storage of hydrogen fuel as a supercold cryogenic liquid is critical to the decarbonisation of the global aviation sector and other hard-to-decarbonised industries. To power future aircraft using hydrogen will require lightweight storage technologies to store liquid hydrogen at $-252℃$ [1, 2]. Fibre reinforced composites, particularly those made of carbon fibres, are a promising solution for this challenge, offering up to 40% weight reduction over metallic tanks. However, existing aerospace-grade carbon fibre composites have been found to suffer matrix microcracking in the thickness direction of laminates, and these microcracks can link up to form interconnected pathways for hydrogen gas to escape [3-5]. To

address this problem, nano-toughening techniques have been found effective in improving the microcracking resistance of epoxy-based carbon fibre composites at cryogenic temperatures [6-9]. However, epoxy or thermoset polymer-based composites are more challenging to recycle or re-manufacture than thermoplastic composites [10-14]. In addition, thermoplastic composites have the added advantage of being made by direct three-dimensional (3D) printing, offering a more rapid manufacturing process.

Although thermoplastic composites have been successfully manufactured using 3D printing [15-19], there is a lack of understanding of their structural performance at cryogenic temperatures, especially their propensity to matrix cracking due to thermal residual stresses and mechanical loads [3]. 3D printing of continuous carbon fibre reinforced thermoplastic composites, herein denoted as 3D-printed composites, offers a new route for manufacturing intricate designs and cylindrical vessels as shown in Fig. 1. However, as-printed composites are known to contain high level of voids due to the entrapment of air between successive printed beads or filaments [16-21]. Furthermore, they suffer from high residual thermal stresses stemming from the temperature discrepancies between the filaments extruded from the nozzle and the printed part [21]. Recent research has shown that these issues can be addressed through heat treatments [22, 23]. However, it remains unknown how the voids affect the initiation and growth of microcracks and whether heat treatments can improve the composite's resistance to microcracking when subjected to the typical thermomechanical environment of liquid hydrogen vessels.

To address these gaps, this study aims to elucidate the microcracking resistance of a 3D-printed thermoplastic composite with a particular focus on understanding the influences of voids and residual thermal stresses resulting from 3D printing on the microcracking behaviour observed at cryogenic temperatures. 3D printed composites were produced using a continuous fibre 3D printer, Markforged® X7 from the USA, which employs the fused filament fabrication (FFF) process to extrude carbon fibre reinforced nylon filaments and deposit them on a bed at an elevated temperature. Optical microscopy was employed to study the voids in as-printed composites and after heat treatment. Three-point bending tests were conducted to assess the microcracking resistance of the as-printed and heat-treated composites at room and cryogenic temperatures.

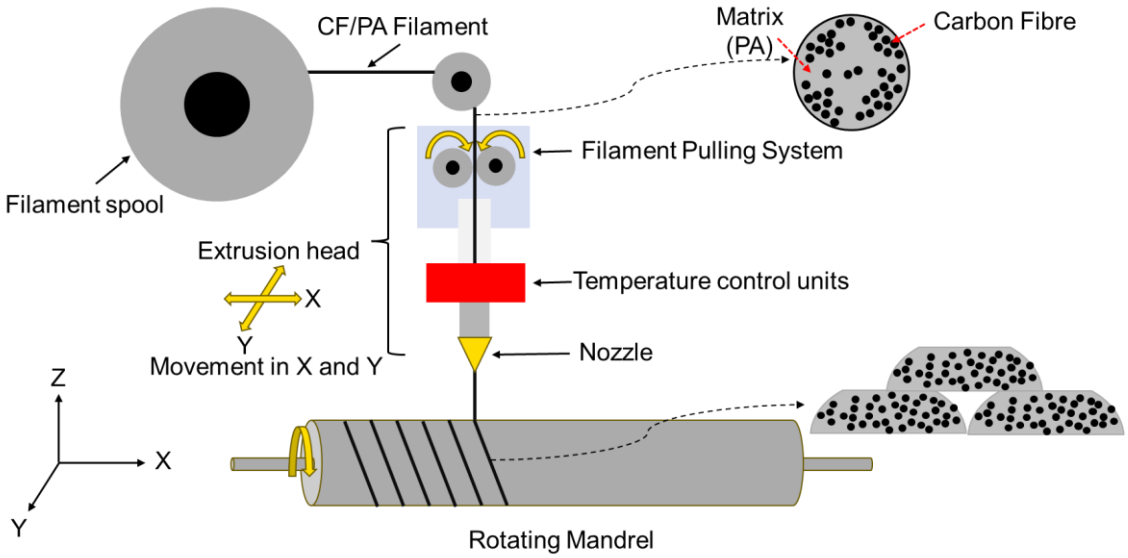

Fig. 1 3D printing of a thermoplastic composite vessel for storing cryogenic liquids.

2.Experimental

2.1. Manufacturing, heat treatment, and materials

Two filament materials were employed, including a short-carbon-fibre (SCF) reinforced nylon 6 filament and a continuous-carbon-fibre (CCF) reinforced nylon filament from Markforged®, USA; the product codes are SCF F-MF-0001 and F-MT-CFVX, respectively. The short-fibre filament was used to print the external surface layers while the interior of the composite was made using the continuous fibre filament. Printing of the two different filaments was carried out with different nozzles, with the nozzle temperatures being set at 270°C for SCF filament 252°C for the CCF filament, respectively. The chamber temperature of the print bed was maintained at room temperature. During the extrusion process, the temperature of the extruded CCF filament decreased swiftly from its nozzle temperature to approximately 100°C just above the already printed section, as documented in previous literature [22]. As a result, the stress-free temperature of the melted filament directly above the printed portion was approximately 100°C.

The heat treatment of the printed CFRP composites was aimed at reducing porosity, employing a dual approach involving vacuum sealing and positive pressure within an autoclave. The composites were placed between two metal plates to ensure their flatness for subsequent mechanical testing. Two PTFE films were inserted between the composite and the plates to aid in their retrieval post-treatment. The assembly was vacuum sealed within a vacuum bag and subsequently placed in an autoclave, where it underwent pressurization to two bars using nitrogen gas. The heat treatment protocol involved a gradual heating rate of 10°C/min, starting from 25°C and reaching 180°C, and a hold time of 1 h at the peak temperature, followed by a controlled cooling at the same rate to 25°C. Since the peak temperature was above the glass

transition temperature of the matrix, the heat treatment effectively reset the stress-free temperature to 180°C, substantially above that of the as-printed composites.

2.2 Characterization methods

The microstructures of both the CCF and SCF filaments, as well as the resulting printed parts, were studied using an optical microscope (ZEISS Axio Zoom) at various magnifications (×10, ×50, ×100). Image analyses to evaluate porosity were carried out using ImageJ software. Pores in the images were distinctly color-coded. After the images were converted to binary format, the software calculated the areas represented by the black regions. For each analysis, ten images from each system were used.

The Mettler-Toledo Thermal Analysis device (STARe System) was used for Dynamic Scanning Calorimetry (DSC) to identify the specific polyamide in the CCF and SCF filaments. An initial heating rate of 10°C/min was used to heat the samples from 25°C to 300°C to eliminate any prior thermal history. The samples were then cooled back to 25°C at the same rate. Another identical temperature ramp was performed to evaluate key thermal properties of the polymer, such as the Glass transition temperature (T_g), melting temperature (T_m), crystallization temperature (T_c), and enthalpy. Results from the thermograms suggest that the CCF filaments' matrix is polyamide 6-I (PA6-I), whereas the SCF filaments' matrix is polyamide 6 (PA6).

The ply cracking behaviour of the CFRP composites was evaluated using a three-point bending test, conducted both at room temperature (RT) and cryogenic temperature (CT), denoted as liquid nitrogen temperature (-196°C). A minimum of three samples were tested for each condition. The 3D-printed CFRP composite samples measured 153.6 mm in length, 13 mm in width, and 4 mm in thickness, with a nominal ply thickness of 0.125 mm. To ensure structural integrity during printing [24], four SCF layers were printed at both the top and bottom surfaces of the samples, as well as around the perimeter of each printed CCF layer. These specific layers are termed "roof & floor layers" and "wall layers," prevented part breakage and detachment during the printing process. Between the roof and floor layers, CCF layers were printed with a stacking sequence of $[90_6/0_{12}/90_6]$, where the 0° fibre orientation aligned with sample's length. During the three-point bending tests, the top surfaces of the sample were under compression while the bottom surface were under tension. The peak tensile strain in the CCF layer furthest away from the mid-plane of the composite can be calculated using the formula, $\varepsilon = 6\delta h/L^2$, where ε denotes the maximum strain in continuous fibre layer on the tension side, δ the mid-span deflection, L the span length, and h the thickness of beam, excluding the roof and floor layers.

3. Experimental results

The results of the microstructural, thermal, and mechanical characteristics of the filaments and the 3D printed composites, before and after heat treatment, are presented and discussed below.

3.1 Microstructures and differential scanning calorimetry of the filaments

The microstructures and thermal properties of both CCF and SCF filaments were analyzed to determine the distribution of carbon fibres, the shape and presence of voids, and the composition of the matrix.

Fig.2 illustrates the microstructures of the (a-b) CCF and (c-d) SCF filaments, as well as the DSC results for both filaments during the (e) initial and (f) subsequent temperature cycles. This temperature cycle involved a ramp from 25°C to 300°C at a rate of 10°C/min, a 5-minute hold, and then a cooling phase back to 25°C at the same rate. The CCF filaments consist of CCF embedded within a polyamide matrix, while SCF filaments have SCF within a polyamide 6 matrix. A more detailed discussion on the matrices of these two filaments will follow later. The diameters for the CCF and SCF filaments are approximately 380μm and 1720μm, respectively. The individual carbon fibre diameter in both filaments is around 7μm, within the normal range of 5-10μm.

Observations from Fig.2a-b indicate that CCF distribution is not even, with areas being rich in either fibre or matrix. There are also visible voids in the filaments. The measured porosity and fibre volume fraction for the CCF filament were about 1.14% and 26.32%, respectively, using Image-J. This aligns closely with data from existing literature [26]. Conversely, the SCF filaments, as displayed in Fig.2c-d, exhibited an even distribution of SCF without any noticeable voids. The purpose of the DSC analysis for both filaments was to determine the characteristics of their matrix materials. The initial heating-cooling cycle aimed to eliminate the filaments' thermal history. As illustrated in Fig.2e, during the heating phase, the SCF filaments displayed a melting temperature (T_m) of approximately 202℃ and a crystallization temperature (T_c) of 161℃ in the cooling phase. This solidified the fact that the SCF filament's matrix is polyamide 6, which aligns well with findings from literature references [27, 28].

On the other hand, the CCF filaments, during the initial heating-cooling cycle, presented a glass transition temperature (T_g) of roughly 72℃ in the heating stage and lacked a discernible endothermic peak, indicating an absence of a distinct melting point. Fig.2f shows that, in the subsequent heating-cooling cycle, the SCF filaments had a similar T_m of 202℃ during heating and a T_c of 164℃ upon cooling, underscoring the matrix of SCF as semi-crystalline nylon (polyamide 6). In the same cycle for the CCF filaments, a T_g of 123℃ was determined during heating, and again, no evident endothermic peak was seen, suggesting the matrix of the CCF filament to be the semi-aromatic polyamide 6-I, as reported in [26].

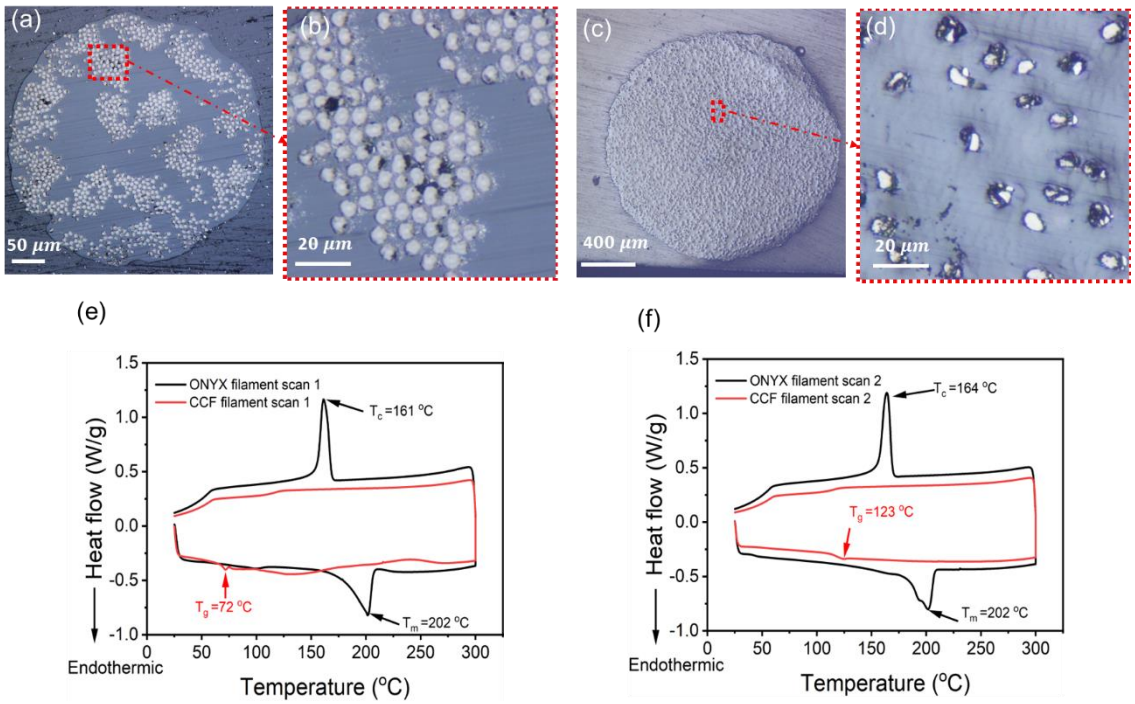

Fig. 2 Microstructural images of (a-b) CCF and (c-d) SCF filaments, alongside DSC results for CCF and SCF filaments during (e) the initial and (f) subsequent heating-cooling cycles. The temperature ramped from 25 ℃ to 300 ℃ at a rate of 10 ℃/min, held for 5 minutes, and then cooled back to 25 ℃ at 10 ℃/min.

Fig. 3 presents microstructures of the (a) 3D printed composites alongside (b) a detailed schematic illustrating layer thicknesses and magnified views of the (c) SCF layer, (d) 0° layers, and (e) 90° layers. The composite's printed layer thickness is consistently 0.125 mm. As indicated in Fig.3b, both the top and bottom of the composite consist of four SCF layers, amounting to a total thickness of 0.5 mm. Sandwiched between these layers, the fibre stacking follows a $[90_6/0_{12}/90_6]$ sequence, which translates to thicknesses of 0.75 mm, 1.5 mm, and 0.75 mm for each respective ply.

A detailed examination of the top and bottom SCF layers reveals uniformly distributed short carbon fibres, as depicted in Fig.3c. However, the middle 0° and 90° CCF layers, shown in Fig.3d-e, exhibit noticeable voids. These voids stem from air being entrapped between individual beads during the printing process [26, 29-31]. The voids in the 0° layer were elongated in shape, while those in the 90° layer appeared to be elliptical, recurring at approximately 4 mm intervals between each bead. This formation is likely a result of the high viscosity of nylon resin, which occurs at a relatively low temperature due to the quick cooling of the filament during the printing process. Image analysis indicate that the porosity level of the 3D printed CFRP composites stands at approximately 14.6%. Such substantial porosity can be attributed mainly to insufficient overlap between neighbouring print beads and layers. Although a printed bead tends to flatten post-deposition, it doesn't always effectively fill the space between adjacent beads due the high viscosity, as discussed in [17, 32].

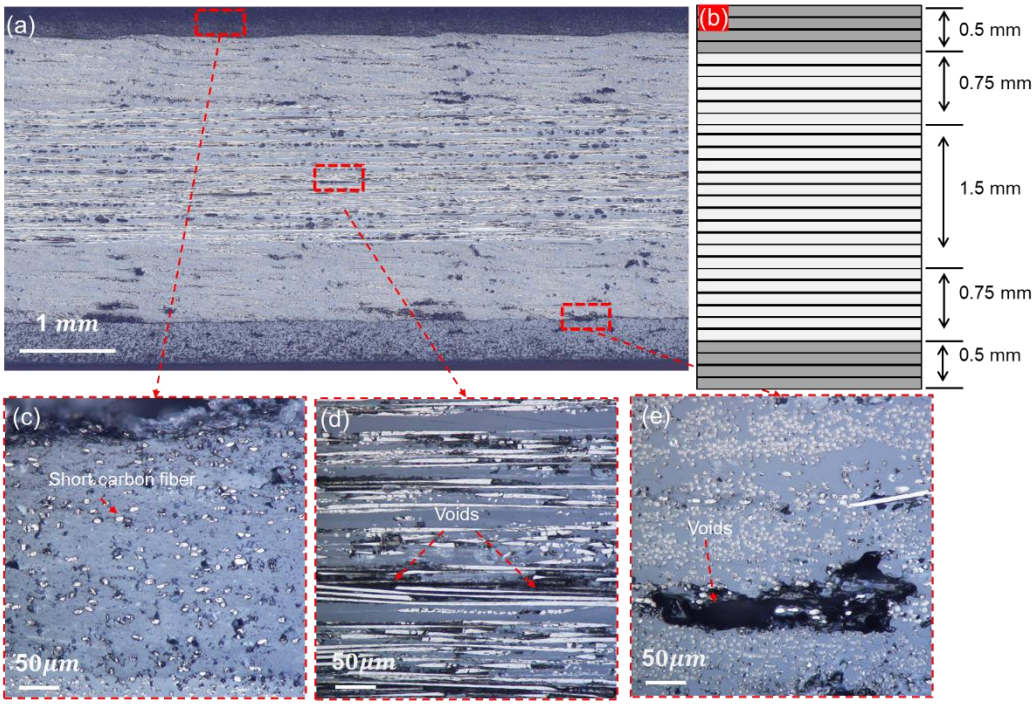

Fig. 3 Microstructures of the (a) 3D printed CFRP composites, (b) their schematic representation, and magnified views of the (c) SCF layer, (d) 0° layers, and (e) 90° layers.

3.2 Microcracking in composites at different temperatures

Three-point bending tests were performed on the 3D printed composite under both room RT and CT conditions. Using a digital microscope, the crack length was monitored during crack growth at different strain levels. Crack developments at RT and CT are illustrated in Fig. 4 and Fig. 5, respectively.

The schematic representation and experimental setup of the three-point bending is shown in Fig. 4a-b. The location of peak strain is indicated in Fig. 4a, at the mid-span's lowest point. Prior to the application of bending load, the as-printed composites were free of any cracks, as shown in Fig. 4c, with only the voids caused by trapped air during the printing process visible. As the peak strain increased to 1.75%, microcracks were observed in Fig.4d, resulting from the amalgamation of several fibre-matrix debondings due to stress concentration at their interface [9]. When the peak strain reached 2.25%, as shown in Fig. 4e, the microcracks grew in length, and extended through the thickness of the 90° layer when the peak strain reached 2.75% (Fig. 4f). Upon reaching the interface with the 0° ply, the ply crack caused a delamination to develop at the ply interface.

The schematic and experimental setup of the three-point bending under the liquid nitrogen bath are presented in Fig. 5a-b. Upon quenching the specimens to CT but prior to applying any mechanical load (0.0% strain), no discernible microcracks could be observed in either the 0° or 90° plies, as depicted in Fig. 5c. This observation suggests that immersing the 3D-printed composite in a cryogenic liquid doesn't cause matrix cracking. This is in stark contrast with carbon fibre reinforced epoxy composites, which were reported to display full-thickness matrix cracks along the fibre direction at cryogenic temperatures [7, 25]. Furthermore, even as the applied strain reached 0.40%, as seen in Fig.5d, no crack could be found. When the applied

strain increased to 0.6%, through-thickness cracks in the 90° ply became evident. As depicted in Fig. 5e, two inclined cracks emanating from a void, Fig. 5f, were seen in the 90° ply, and a through-thickness crack was visible in the SCF layer.

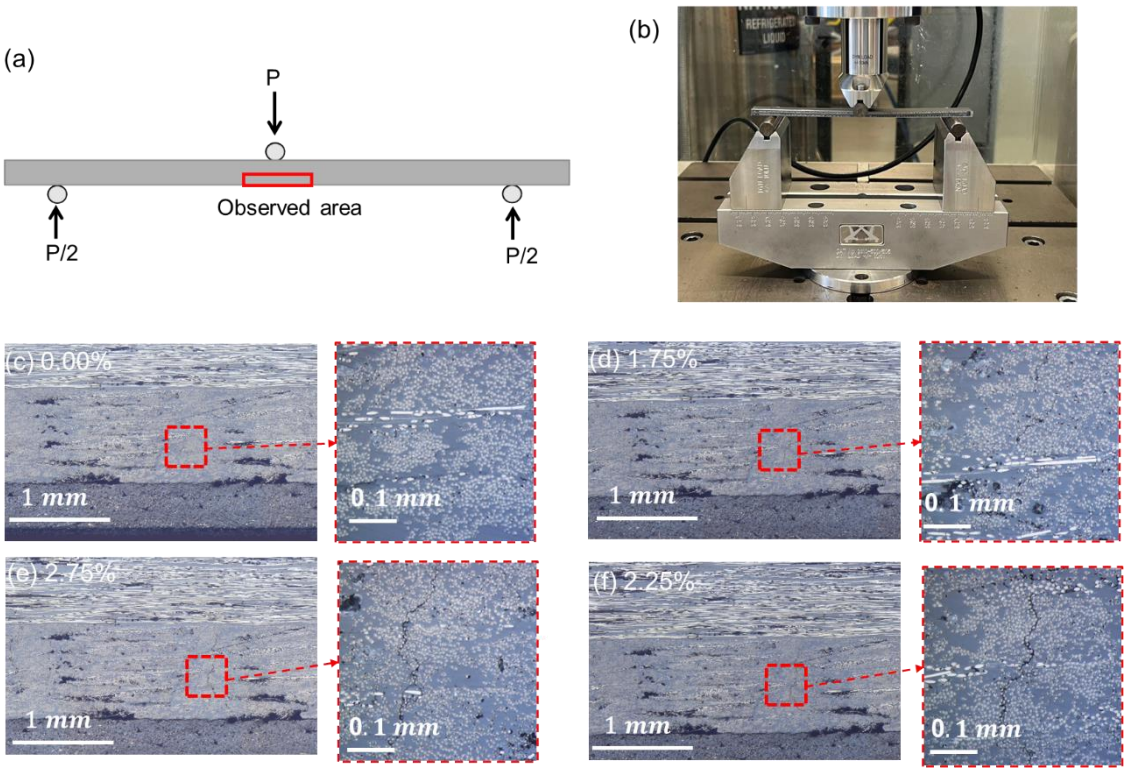

Fig. 4 (a) Schematic representation and (b) experimental setup of the three-point bending test at room temperature, with emphasis on the calculated strain. Following are the microcracking of the 3D-printed CFRP composite after three bending tests at RT for different strains: (c) 0.00%, (d) 1.75%, (e) 2.25%, and (f) 2.75%.

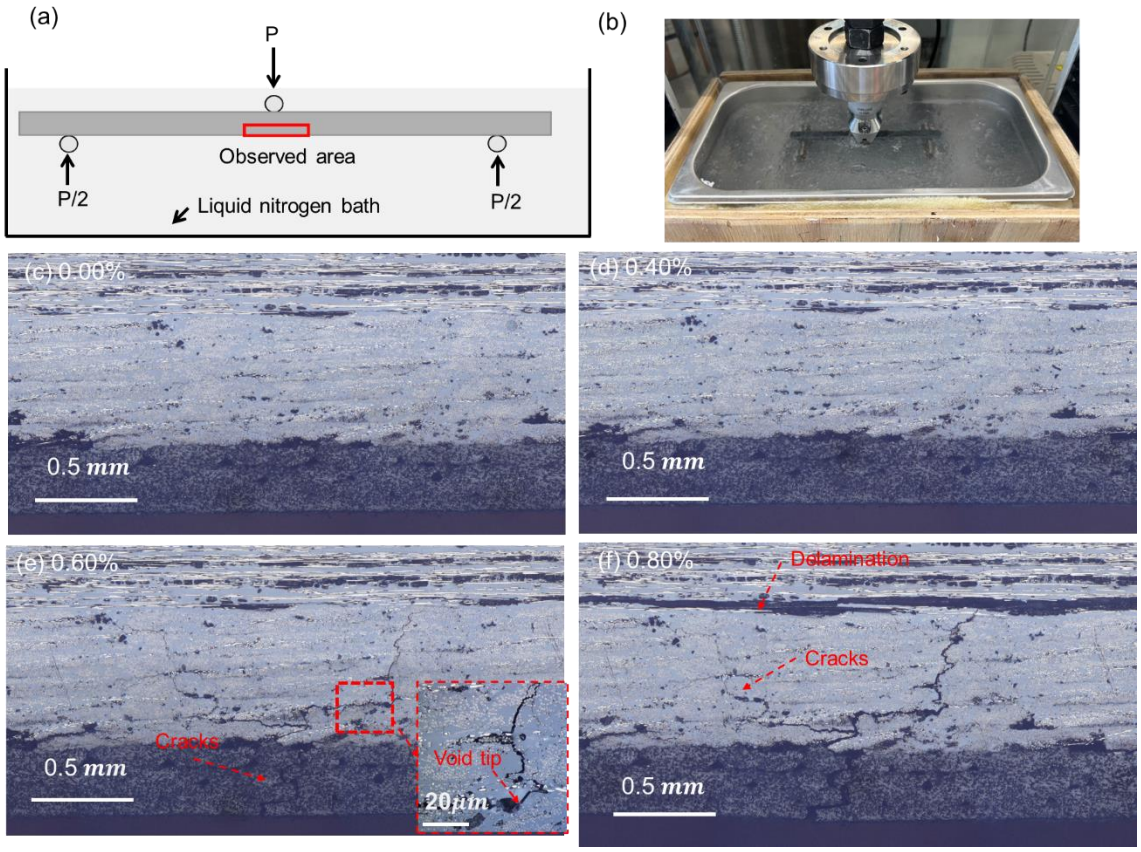

Fig. 5 (a) Schematic representation and (b) experimental setup of three point bending test at cryogenic temperature. Microcracking of the 3D-printed CFRP composite following three bending tests at cryogenic temperature for varying strains: (c) 0.00%, (d) 0.40%, (e) 0.6%, and (f) 0.8%.

3.3 Effect of heat treatment on microcracking resistance

Since the microcracks observed in the 3D printed composites were linked to voids, it is important to understand whether the composites' resistance to through-thickness microcracking can be enhanced by reducing the voids through heat treatment. In addition to closing voids, heat treatment may also improve the bond strength between carbon fibres and the nylon matrix.

Fig.6 depicts the microstructure of the heat-treated 3D printed CFRP composites. It is clear the that compared the as-printed composite, the heat-treated composite was found to have significantly lower porosity of about 0.26%. As illustrated in Fig.6a-b, the sample's overall thickness decreased from 4 mm to 3 mm. This thickness reduction predominantly occurred because the matrix of the 0° layer was compressed, reducing its thickness from 1.50 mm to 0.78 mm. Meanwhile, the thicknesses of the 90° layers and the SCF layers remained largely unaffected. As shown in Fig.6c-e, the elliptical voids in both the 0° and 90° layers of as-printed composites seem to have vanished, leaving behind only smaller size round voids, likely due to trapped air within the voids be absorbed by the matrix, although further investigation is necessary to ascertain the primary mechanism.

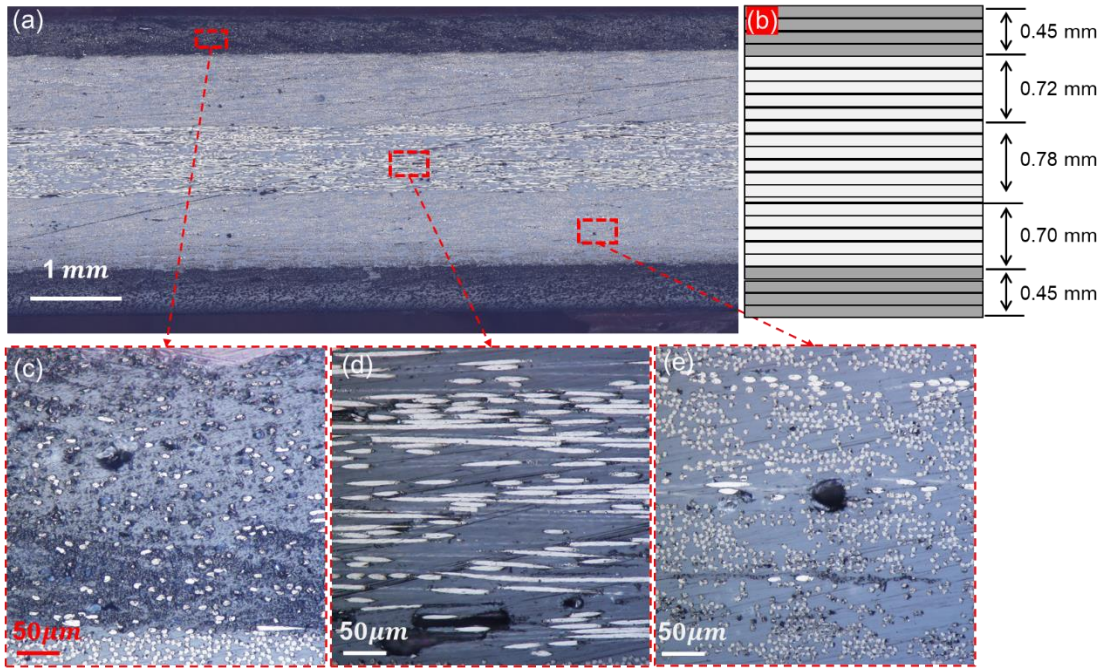

Fig. 6 Microcracking of the 3D-printed CFRP composites: (a) after heat treatment and (b) its schematic representation. Detailed views are presented for the (c) SCF layer, (d) 0° layers, and (e) 90° layers.

Fig. 7 shows the microcrack of the heat-treated sample under three-point bending at CT. As shown in Fig. 7a, when the applied strain was increased to 0.20%, no crack was observed . However, a through-thickness crack and delamination crack were seen in the composite when the strain was increased to 0.40% (Fig. 7b). The transverse crack with zig-zag shape was nearly perpendicular to the loading direction. The crack deflected at resin-rich areas. Thus, the ply cracking strain for the heat-treated sample was 0.40%.

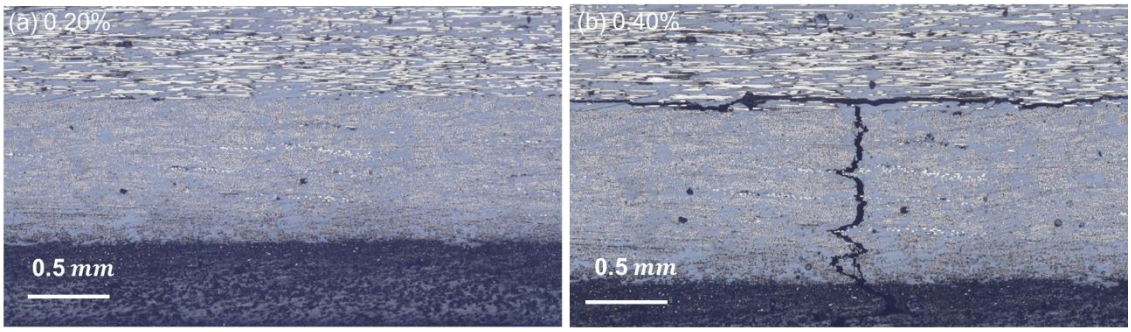

Fig. 7 Microcracking of the heat-treated 3D-printed CFRP composite post three bending tests at cryogenic temperature under specific strains: (a) 0.20%, and (b) 0.40%.

4. Finite element analysis modelling

To elucidate the unexpected reduction in the composite's resistance to microcracking following heat treatment under external mechanical load, finite element analysis was conducted. The

analysis aimed to ascertain the rise in thermal residual stresses and ascertain whether this factor is responsible for the observed decrease in ply cracking strain.

Finite element analysis (FEA) was conducted using ABAQUS/Explicit 2021, adopting the micromechanical model described in [9]. This model was employed to investigate the matrix cracking phenomenon in the 3D printed CFRP composite when subjected to mechanical loading at both room temperature (RT) and cryogenic temperature (CT). Fig. 8 shows the finite element model of a 3D printed CFRP composite with a stacking sequence of $[90_6/0_{12}/90_6]$. The schematic representation and its micromechanical model were shown in Fig.8a-b. In the micromechanical model, boundary conditions and periodic constraints were implemented using a linear multi-point constraint approach as detailed in [9]. To achieve a specific tensile strain ε_{xx}, a displacement of $\varepsilon_{xx}L$, where L signifies the length in the x direction, was applied to a reference point, as illustrated in Fig.8b. To account for thermal residual stresses, an isothermal analysis step was undertaken prior to applying the mechanical load as described in [25]. The temperature difference, ΔT, set throughout the composite in an isothermal analysis step, signifies the temperature variation between the test temperature and the stress-free temperature. As outlined in Sections 2.1 and 2.4, the stress-free temperatures for the as-printed and heat-treated samples were 100°C and 180°C, respectively, while the test temperatures were 25°C for RT and -196°C for CT, respectively. Therefore, the temperature variation ΔT for the as-printed and heat-treated samples at CT was -296°C and -376°C, respectively. The material properties of the carbon fibres, matrix, fibre-matrix interface and the homogenized 0° ply are summarised in Tables 1, 2, 3 and 4.

Initially, a thermal analysis was first performed using the model where temperature variations of -296°C and -376°C were applied, simulating the conditions experienced by the as-printed and heat-treated composites during testing at the cryogenic temperature. The properties of the 0° and 90° plies are determined using laminate theory based on the properties of the carbon fibres and epoxy resin listed in Tables 1 and 2.

The combined thermomechanical loadings are illustrated in Fig.8c. Schematics of material constitutive models are shown in Fig.8d. The micromechanical model for the 90° layer comprises three components: the polyamide 6I matrix, carbon fibres, and the interfaces between the fibres and the matrix. The polyamide 6I matrix is modelled as an elastic-plastic material with a bilinear continuum damage law. The carbon fibres are assumed to be transversely isotropic with linear elasticity. The interface between fibres and matrix is described by a bilinear cohesive zone model (CZM). Homogenized 0° ply material was at the top and the edge of the 90° layer had a symmetric boundary condition. The outer 0° ply layer is represented as a linear-elastic, orthotropic solid with the homogenized stiffness pertinent to that of 0° ply [9].

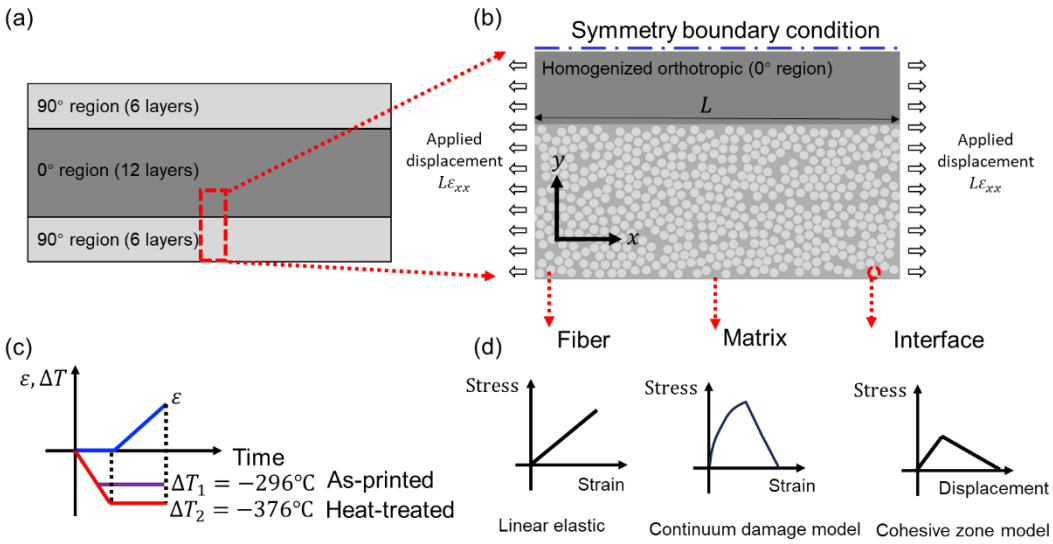

Fig. 8 Finite element modelling of 3D printed composite. (a) A laminate model. (b) A micromechanical model. (c) Loading conditions. (d) Material constitutive relationships.

The modelling results of as-printed samples at RT (Fig. 9) and CT (Fig. 10) under three points bending are discussed below. Fig. 9a showed the 90^0 layers under the unloaded conditions. As shown in Fig. 9b, when the strain was increased to 1.75%, disbonds were seen between some carbon fibres and the matrix. Further increasing the strain to 2.33%, a clearly visible crack was observed in Fig. 9c, which then extended through the thickness of the ply when the applied strain reached 2.75%, referring to Fig. 9d.

Similarly, the crack initiation and propagation results of the 3D printed composite at CT are shown in Fig. 10. Debondings between carbon fibres and the matrix occurred at a strain of 0.55% (Fig. 10b). Crack propagation was observed at the strain of 0.64% (Fig. 10 c), forming a through-thickness crack when the applied strain was increased to 0.70% (Fig. 10d).

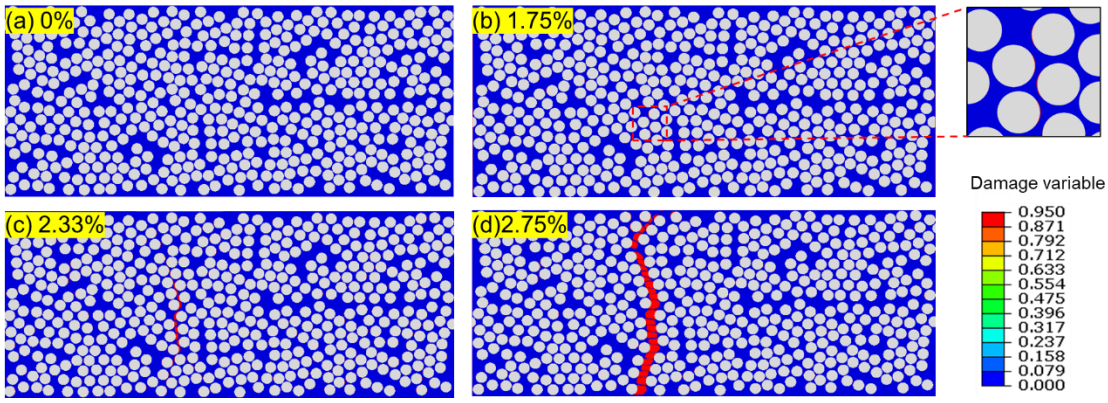

Fig. 9 Microcracking modelling of the 3D-printed CFRP composite after three bending tests at RT for different strains: (a) 0.00%, (b) 1.75%, (c) 2.33%, and (d) 2.75%.

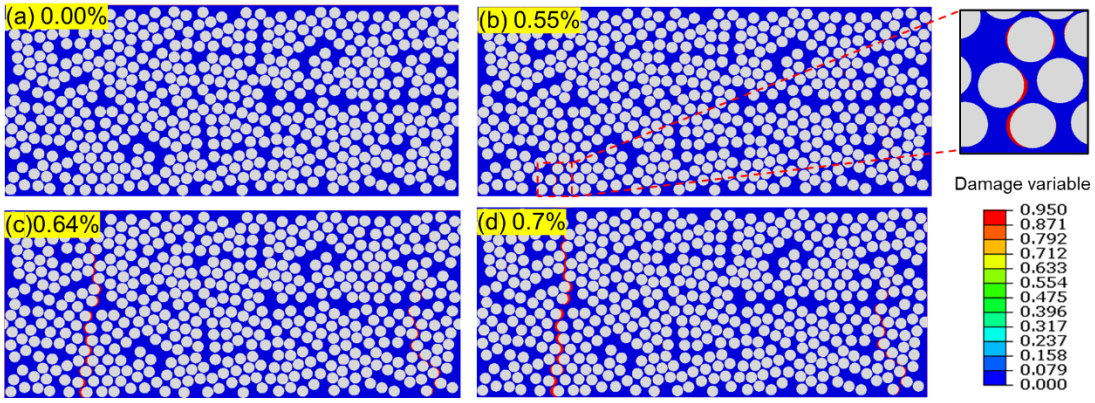

Fig. 10 Microcracking modelling of the 3D-printed composite after three bending tests at CT for different strains: (a) 0.00%, (b) 0.55%, (c) 0.64%, and (d) 0.70%.

Many studies have reported that heat treatment (annealing) can improve the mechanical properties of 3D printed composites through reduced porosity by infiltration and diffusion among adjacent filaments and layers and interface strengthening [23, 33, 34]. Thus, the ply cracking strain of 3D printed composite was expected to increase because of the reduced void areas after heat treatment compared to that of the as-printed sample. However, the present results show that the heat-treatment composites displayed a lower ply splitting strain than their as-printed counterpart. This could be attributed to the heat treatment process that resulted in higher thermal residual stresses than in the as-printed composite. The computational results reveal that the heated-treated composite was found to experience a higher thermal residual stress than the as-printed composites. The average ply stress in the 90° plies, referring to Fig. 11(a), increased from 55 MPa to 70 MPa, as shown in Fig. 11(b).

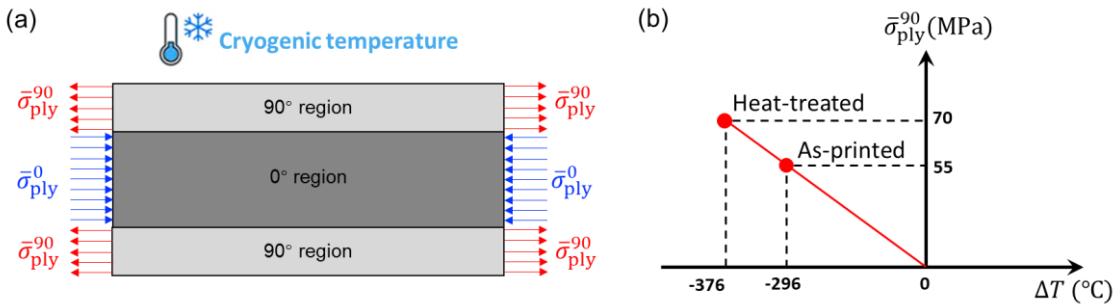

Fig. 11 Effect of Heat Treatment on Microcracking in 3D Printed Composites. (a) Schematic representation of thermal residual stress distribution within the composite layers at cryogenic temperatures. (b) Relationship between thermal residual stress and temperature difference.

By accounting for the higher thermal residual stress in the micromechanical model, leading to a reduced ply cracking strain, which is the specific strain threshold where normalized crack length reaches unity. The heat treatment results in a composite structure more susceptible to the initiation of ply cracking at lower strains. The data presented in Fig. 12, with experimental results harmonizing with the model's predictions, underscore this phenomenon. At the juncture

where the normalized crack length equals one, the heat-treated composite reaches this critical point at a markedly lower strain compared to the as-printed counterpart, affirming the hypothesis that heat treatment, while beneficial in certain aspects, can inadvertently elevate the thermal residual stress, thereby diminishing the material's resistance to ply cracking under cryogenic conditions.

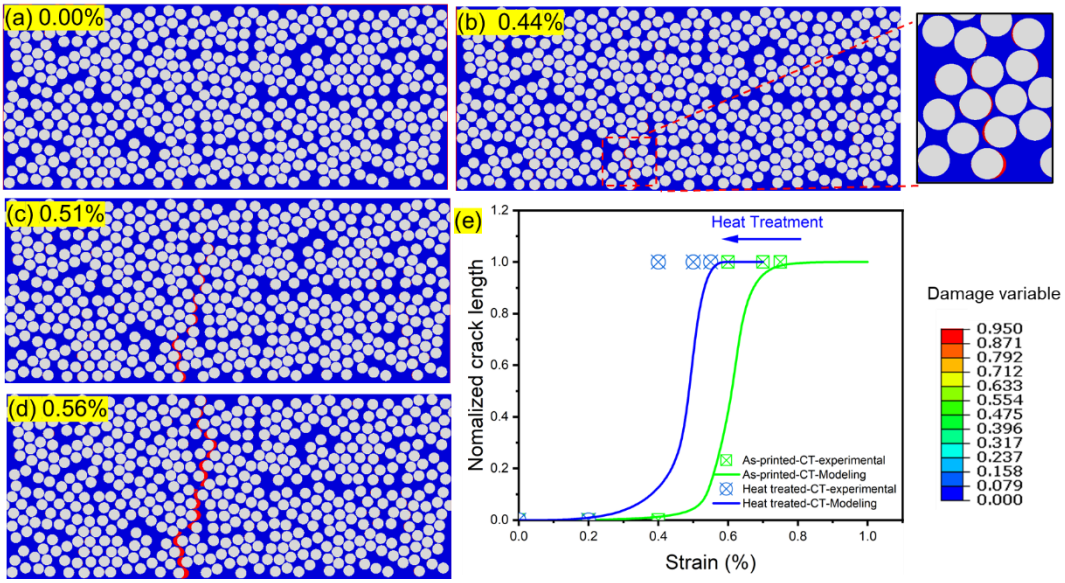

Fig. 12 Microcracking modelling of the heat-treated 3D-printed composite post three bending tests at cryogenic temperature under specific strains: (a) 0.00%, (b) 0.44%, (c) 0.51% and (d) 0.56% and (e) Normalized crack lengths as a function of strain for as-printed and heat-treated composites at room and cryogenic temperatures, juxtaposing experimental data with model predictions.

Having now determined the thermal residual stresses, they can be employed in the micromechanical model for the heat-treated composite; the results are presented in Fig. 12(e). Similarly, debondings between carbon fibres and the matrix occurred at a strain of 0.44% (Fig. 12b). Cracks then propagated to stably as the applied strain was increased 0.51% (Fig. 12c), finally forming a through-thickness crack as the strain reached 0.56% (Fig. 12d).

4. Discussion

A comparison of the model predictions and experimental results of crack length versus strain for the as-printed composite at RT and CT, and the heat-treated composite at CT is presented in Fig. 13. The normalized crack length, i.e., the crack length divided by the thickness of the 90° layer, is presented in Fig. 13a, together with the prediction of the micro-mechanical model. Herein, the critical strains when the matrix crack spans the full thickness of the 90° layer is denoted as the ply cracking strain. All the experimental results were compared to the modelling results as shown in Fig. 13a. It is clear that the model predictions are in good agreement with the experimental results.

For the 3D printed CFRP composite at RT, the ply cracking strain was found to be 2.75%. By contrast, carbon fibre reinforced epoxy composites at RT were reported to feature a ply

cracking strain ranging from 0.6% to 0.8% [9, 33-36]. The notably higher ply cracking strain of the 3D printed CFRP composite (2.75%) can be attributed to the superior fracture toughness of its nylon matrix, which boasts an estimated fracture toughness of 7 kJ/m^2 [37], particularly when compared to the epoxy's 0.12 kJ/m^2 [8, 25] at RT. The normalized crack length versus strain for the 3D printed CFRP composite at CT, as also shown in Fig. 13a together the model prediction, suggest that the ply cracking strain for this composite at CT was around 0.6%.

Comparing the results of RT and CT, it is clear that the ply cracking strain of the 3D printed CFRP composite dropped from 2.75% at RT to 0.6% at CT, largely due to the much lower fracture toughness of nylon at CT. By comparison, epoxy-based carbon fibre reinforced composites typically exhibit a ply cracking strain around 0%, viz. through-thickness matrix cracks would form upon immersing the composite in cryogenic liquids. The vulnerability of epoxy-based composites is primarily due to epoxy having a very low fracture toughness of 0.06 kJ/m^2 at CT [8, 25].

Additionally, it's worth pointing out that heat treatment can effectively lower the porosity of 3D printed CFRP composite from 14.59% to 0.26%. However, such heat treatment did not increase the ply cracking strain at CT. Instead, the ply cracking strain dropped from 0.6% to 0.4%, as depicted in Fig. 13b. This unexpected reduction is mainly attributed to the increased thermal residual stress following heat treatment. As discussed earlier, after heat treatment the stress-free temperature of the composites increased to 180 ℃, causing the composite to experience a higher thermal residual stress at CT than the as-printed composite. This new understanding paves the way for applications of the cryogenic composite vessel using the 3D printing technology as shown in Fig. 1.

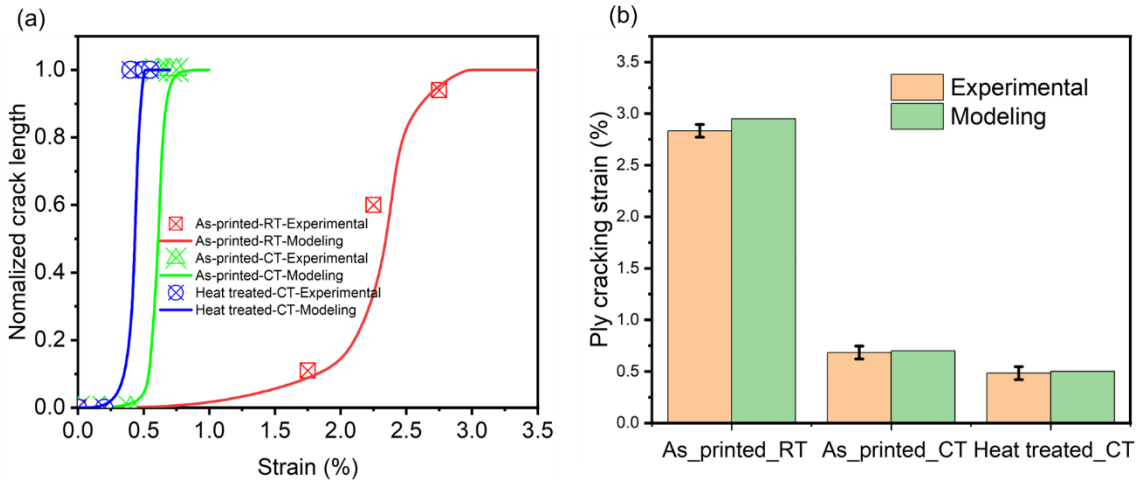

Fig. 13 A comparison of experimental results 3D printed composite at room and cryogenic temperatures, with and without heat treatment. (a) Normalised crack lengths with increasing strain, and (b) ply cracking strain of as-printed and heat-treated composites at both RT and CT.

5. Conclusion

The microcracking behavior of the 3D printed carbon fibre reinforced thermoplastic composites has been characterized by three-point bending under room and crogenic temperatures. The results showed that the 3D printed composites exhibit significantly higher ply cracking strain (around 2.75% and 0.6% at RT and CT respectively) than epoxy-based carbon fibre reinforced composite (typically between 0.6% and 0.8% and 0.0% at RT and CT, respectively). Heat treatment has been found to effectively reduce the porosity of the 3D printed CFRP composites from 14.59% to 0.26%. However, such heat treatment unexpectedly caused a slight decrease in the ply cracking strain of the 3D printed composites, from 0.6% to 0.4%. This reduction is most likely due to heat treatment raising the stress-free temperature, and hence increasing thermal residual stress at cryogenic temperatures. A micro-mechanical model has been developed to understand the micro-cracking behavior of the as-printed and heat-treated composites. After accounting for the effects of thermal residual stresses, the model's predictions are in good correlation with the experimental results. The findings of this study reveal 3D printing thermoplastic composites offer a promising technique for manufacturing lightweight vessels for storing liquid hydrogen.

Declaration of Competing Interest

The authors declare that they have no known competing financial interests or personal relationships that could have appeared to influence the work reported in this paper.

Acknowledgements

This work was sponsored by the Space Research Network (SRN) pilot project (RG220491).

Table 1. Carbon fibre properties [9]

Material property	Value
Longitudinal Young's modulus (GPa)	279
Transverse Young's modulus (GPa)	15
In-plane Poisson's ratio	0.2
Longitudinal shear modulus (MPa)	15000
Transverse shear modulus (MPa)	7000
Longitudinal CTE (K^{-1})	-1×10^{-6}
Transverse CTE (K^{-1})	5×10^{-6}
Density (g/cm^3)	1.79

Table 2. Matrix properties [38-42]

Material property	**Value at RT**	**Value at CT**

Young's modulus (GPa)	1.28 [40]	5.63 [40]
Poisson's ratio	0.35[39]	0.35[39]
Fracture energy $(\mathbf{J/m^2})$	400 [41]	200*
Tensile strength (MPa)	46 [40]	45.8 [40]
CTE K-1	6.5×10^{-5}	6.5×10^{-5}
Density g/cm3	1.1 [38]	1.1 [38]
***Note: assume fracture energies at CT is half of value of the fracture energies at RT.**		

Table 3. Fibre–matrix interface properties used for the cohesive zone model [43]

Material property	**Value at RT[43]**	**Value at CT**
Penalty stiffness (MPa)	10^8	10^8
Mode-I interface strength (MPa)	76	76
Mode-II, III interface strengths (MPa)	70	70
Mode-I interface fracture energy $(\mathbf{J/m^2})$	40	20*
Mode-II, III interface fracture energy $(\mathbf{J/m^2})$	90	45*
Benzeggagh-Kenane law parameter	1.45	1.45
***Note: assume fracture energies at CT is half of value of the fracture energies at RT.**		

Table 4. Homogenized composite properties [44]

Material property	**Value***
Longitudinal Young's modulus (MPa)	150000
Transverse Young's modulus (MPa)	7500
In-plane Poisson's ratio	0.32
Longitudinal shear modulus (MPa)	3900
Transverse shear modulus (MPa)	2300
Longitudinal CTE (K^{-1})	-1.17×10^{-7}
Transverse CTE (K^{-1})	2.75×10^{-5}
Density (g/cm^3)	1.59

***Note: determined by the FE homogenization of a micromechanical RVE, as in [44].**

Reference

[1] Bouckaert S, Pales AF, McGlade C, Remme U, Wanner B, Varro L, et al. Net zero by 2050: A roadmap for the global energy sector. 2021.
[2] Airbus reveals hydrogen-powered zero-emission engine. 2022.
[3] Nairn JA. Matrix microcracking in composites. Polymer matrix composites. 2000;2:403-32.
[4] Timmerman JF, Hayes BS, Seferis JC. Cryogenic microcracking of carbon fiber/epoxy composites: influences of fiber-matrix adhesion. Journal of composite materials. 2003;37(21):1939-50.
[5] Timmerman JF, Tillman MS, Hayes BS, Seferis JC. Matrix and fiber influences on the cryogenic microcracking of carbon fiber/epoxy composites. Composites Part A: Applied Science and Manufacturing. 2002;33(3):323-9.
[6] Hardingham-Gill T. Airbus to test hydrogen-fueled engine on A380 jet. CNN; 2022.
[7] Islam MS, Benninger LF, Pearce G, Wang C-H. Toughening carbon fibre composites at cryogenic temperatures using low-thermal expansion nanoparticles. Composites Part A: Applied Science and Manufacturing. 2021;150:106613.
[8] Chang W, Rose LF, Islam MS, Wu S, Peng S, Huang F, et al. Strengthening and toughening epoxy polymer at cryogenic temperature using cupric oxide nanorods. Composites Science and Technology. 2021;208:108762.
[9] Chang W, Rose LF, Wu S, Kinloch AJ, Wang CH. Increasing crack growth resistance for through-thickness matrix cracking and its role in suppressing ply cracking in thin-ply laminates. Composites Part A: Applied Science and Manufacturing. 2022;163:107219.
[10] Henshaw JM. Recycling and disposal of polymer–matrix composites. ASM handbook. 2001;21:1006-12.
[11] Henshaw JM, Han W, Owens AD. An overview of recycling issues for composite materials. Journal of Thermoplastic Composite Materials. 1996;9(1):4-20.
[12] Krauklis AE, Karl CW, Gagani AI, Jørgensen JK. Composite material recycling technology—state-of-the-art and sustainable development for the 2020s. Journal of Composites Science. 2021;5(1):28.
[13] Yang Y, Boom R, Irion B, Van Heerden D-J, Kuiper P, De Wit H. Recycling of composite materials. Chemical Engineering and Processing: Process Intensification. 2012;51:53-68.
[14] Zhang J, Chevali VS, Wang H, Wang C-H. Current status of carbon fibre and carbon fibre composites recycling. Composites Part B: Engineering. 2020;193:108053.
[15] Goh GD, Yap YL, Agarwala S, Yeong WY. Recent progress in additive manufacturing of fiber reinforced polymer composite. Advanced Materials Technologies. 2019;4(1):1800271.
[16] Dixit N, Jain PK. 3D printed carbon fiber reinforced thermoplastic composites: A review. Materials Today: Proceedings. 2021;43:678-81.
[17] Kabir SF, Mathur K, Seyam A-FM. A critical review on 3D printed continuous fiber-reinforced composites: History, mechanism, materials and properties. Composite Structures. 2020;232:111476.
[18] Sanei SHR, Popescu D. 3D-printed carbon fiber reinforced polymer composites: a systematic review. Journal of Composites Science. 2020;4(3):98.

[19] Van de Werken N, Tekinalp H, Khanbolouki P, Ozcan S, Williams A, Tehrani M. Additively manufactured carbon fiber-reinforced composites: State of the art and perspective. Additive Manufacturing. 2020;31:100962.
[20] Saenz-Castillo D, Martín M, Calvo S, Rodriguez-Lence F, Güemes A. Effect of processing parameters and void content on mechanical properties and NDI of thermoplastic composites. Composites Part A: Applied Science and Manufacturing. 2019;121:308-20.
[21] de Macedo RQ, Ferreira RTL, Jayachandran K. Determination of mechanical properties of FFF 3D printed material by assessing void volume fraction, cooling rate and residual thermal stresses. Rapid Prototyping Journal. 2019;25(10):1661-83.
[22] Saeed K, McIlhagger A, Harkin-Jones E, McGarrigle C, Dixon D, Shar MA, et al. Characterization of continuous carbon fibre reinforced 3D printed polymer composites with varying fibre volume fractions. Composite Structures. 2022;282:115033.
[23] Wang K, Long H, Chen Y, Baniassadi M, Rao Y, Peng Y. Heat-treatment effects on dimensional stability and mechanical properties of 3D printed continuous carbon fiber-reinforced composites. Composites Part A: Applied Science and Manufacturing. 2021;147:106460.
[24] Van Der Klift F, Koga Y, Todoroki A, Ueda M, Hirano Y, Matsuzaki R. 3D printing of continuous carbon fibre reinforced thermo-plastic (CFRTP) tensile test specimens. Open Journal of Composite Materials. 2016;6(01):18.
[25] Islam MS, Chang W, Sha Z, Wang J, Wu S, Rose LF, et al. Mitigating cryogenic microcracking in carbon-fibre reinforced polymer composites using negative thermal-expansion nanoparticles functionalized by a polydopamine coating. Composites Part B: Engineering. 2023;257:110676.
[26] Chabaud G, Castro M, Denoual C, Le Duigou A. Hygromechanical properties of 3D printed continuous carbon and glass fibre reinforced polyamide composite for outdoor structural applications. Additive Manufacturing. 2019;26:94-105.
[27] Klata E, Van de Velde K, Krucińska I. DSC investigations of polyamide 6 in hybrid GF/PA 6 yarns and composites. Polymer testing. 2003;22(8):929-37.
[28] Pascual-González C, San Martín P, Lizarralde I, Fernández A, León A, Lopes C, et al. Post-processing effects on microstructure, interlaminar and thermal properties of 3D printed continuous carbon fibre composites. Composites Part B: Engineering. 2021;210:108652.
[29] Blok LG, Longana ML, Yu H, Woods BK. An investigation into 3D printing of fibre reinforced thermoplastic composites. Additive Manufacturing. 2018;22:176-86.
[30] Karaş B, Smith PJ, Fairclough JPA, Mumtaz K. Additive manufacturing of high density carbon fibre reinforced polymer composites. Additive Manufacturing. 2022;58:103044.
[31] Yang D, Zhang H, Wu J, McCarthy ED. Fibre flow and void formation in 3D printing of short-fibre reinforced thermoplastic composites: An experimental benchmark exercise. Additive Manufacturing. 2021;37:101686.
[32] Oztan C, Karkkainen R, Fittipaldi M, Nygren G, Roberson L, Lane M, et al. Microstructure and mechanical properties of three dimensional-printed continuous fiber composites. Journal of composite materials. 2019;53(2):271-80.
[33] Arteiro A, Catalanotti G, Melro A, Linde P, Camanho PP. Micro-mechanical analysis of the in situ effect in polymer composite laminates. Composite Structures. 2014;116:827-40.
[34] Arteiro A, Catalanotti G, Reinoso J, Linde P, Camanho PP. Simulation of the mechanical response of thin-ply composites: from computational micro-mechanics to structural analysis. Archives of Computational Methods in Engineering. 2019;26:1445-87.
[35] Parvizi A, Bailey J. On multiple transverse cracking in glass fibre epoxy cross-ply laminates. Journal of Materials Science. 1978;13:2131-6.

[36] Saito H, Takeuchi H, Kimpara I. Experimental evaluation of the damage growth restraining in 90 layer of thin-ply CFRP cross-ply laminates. Advanced Composite Materials. 2012;21(1):57-66.
[37] Lim S-H, Dasari A, Yu Z-Z, Mai Y-W, Liu S, Yong MS. Fracture toughness of nylon 6/organoclay/elastomer nanocomposites. Composites Science and Technology. 2007;67(14):2914-23.
[38] Data Sheet of the Markforged_Composites.
[39] Overview of materials for Nylon 6, Unreinforced.
[40] Cruz P, Shoemake E, Adam P, Leachman J. Tensile strengths of polyamide based 3D printed polymers in liquid nitrogen. IOP Conference Series: Materials Science and Engineering: IOP Publishing; 2015. p. 012020.
[41] Okada O, Keskkula H, Paul D. Fracture toughness of nylon-6 blends with maleated rubbers. Journal of Polymer Science Part B: Polymer Physics. 2004;42(9):1739-58.
[42] Valenza A, Geuskens G, Spadaro G. Blends of polyamide 6 and linear low density polyethylene functionalized with methacrylic acid derivatives. European polymer journal. 1997;33(6):957-62.
[43] Sun Q, Meng Z, Zhou G, Lin S-P, Kang H, Keten S, et al. Multi-scale computational analysis of unidirectional carbon fiber reinforced polymer composites under various loading conditions. Composite Structures. 2018;196:30-43.
[44] Naya F, González C, Lopes C, Van der Veen S, Pons F. Computational micromechanics of the transverse and shear behavior of unidirectional fiber reinforced polymers including environmental effects. Composites Part A: Applied Science and Manufacturing. 2017;92:146-57.